This document is complies with the paper:

S. Siriano, A. Tassone, G. Caruso, "Numerical simulation of thin-film MHD flow for non-uniform conductivity walls", Fusion Science and Technology UFST (2021), 10.1080/15361055.2020.1858671

Numerical simulation of thin-film MHD flow for non-uniform conductivity walls

S. Siriano[*], *A. Tassone, G. Caruso*

[1] *DIAEE–Sapienza University of Rome, Corso Vittorio Emanuele II, 244, 00186 Rome, Italy.*

*simone.siriano@uniroma1.it

Abstract: Liquid metals offer unique properties and their use in a nuclear fusion reactor, both as confined flows and free surface flow, is widely studied in the fusion community. The interaction between this conductive fluid and the tokamak magnetic fields leads to Magnetohydrodynamic (MHD) phenomena that influence the flow features. To properly design components that employ liquid metals, it is necessary to accurately predict these features and, although the efforts made in development, a mature code specifically customized to simulate MHD flows is still unavailable. In this work, the general purpose CFD code ANSYS CFX 18.2 is validated for MHD free surface thin film flow with insulated walls, up to $Ha = 1000$ and for several values of the characteristic width/thickness ratio, comparing the results with the theoretical relation available in the literature. For all the cases considered, the maximum integral error is found below 10 %. Successively, the validated code is used to investigate the MHD flow in a chute with a characteristic film ratio equal to 0.1 and for $Ha = 300$. Uniform and non-uniform wall electrical conductivity cases are considered with the latter modelled by placing on the side walls and on the back wall localized regions with different conductivity. The electrical conductivity of the back wall is found to have a negligible effect on the global flow when the lateral wall in insulated, similarly to what is observed for the analogous bounded flow. Contrariwise, an electrically conductive lateral wall is found to enhance the free surface jet and to modify the Hartmann layer structure.

Keywords: CFX; Free-Surface Flow; Magnetohydrodynamics (MHD); Non-uniform electrical conductivity; thin film flow.

1. Introduction Nuclear fusion is the process that powers the Sun and the stars and is considered a sustainable and CO_2-free energy source that could be potentially used to meet the ever-increasing global energy demand. At the extremely high temperature needed to sustain the fusion reaction, the fuel is in the plasma state, that is completely ionized and dissociated in electrons and ions. In 2018, EUROfusion published a document entitled "European Research Roadmap to the Realisation of Fusion Energy" [1] , which outlined 8 key design issues to face the main challenges for the realisation of the first fusion reactor. The "M2. Heat-exhaust systems" mission is on the development of an adequate solution for high thermal loads to which the Plasma-Facing Components (PFCs) are subjected. The baseline strategy for the accomplishment of M2 is to optimize and understand operation with a conventional PFC (water-cooled, metallic armor, Eurofer heatsink) but, in parallel, an aggressive program to develop alternative solutions is necessary [1].

Liquid Metals (LM) have unequaled properties as plasma-facing materials in a fusion reactor because they can be re-circulated and regenerated, enhancing the performances and the lifetime of the components where they are employed. Compared to solid PFCs, LM-PFCs have the potential to provide enhanced power-removal capability, by evaporation and relocating the heat with a flowing stream; offer a "self-healing" surface that is practically free from permanent damage by erosion, neutron-induced swelling and plasma irradiation damage; eliminate issues as thermal stresses, local melting and recrystallization; reduce overall system down-time and repair cost and facilitate tritium production, retention, removal and handling [2–4]. However,

it is still a challenging goal to form a continuously flowing LM film flow with both stable surfaces and uniform thickness due to magnetohydrodynamics (MHD) effects [5].

Since the liquid metals are electrically conductive, their movement is inducing internal currents when happening under an external magnetic field, as it is often the case in a fusion reactor. These currents will interact in turn with the magnetic field resulting in Lorentz forces that can affect both the macroscopic (e.g. velocity and free surface stability), and microscopic flow features (e.g. turbulence). This interaction leads to the development of rich physical phenomena, not encountered in classical fluid dynamics that present a complex coupled interplay of magnetic, inertial, viscous and surface tension forces. Furthermore, the Lorentz force is not uniformly distributed on the channel cross-section but is dependent on the overall magnitude and paths of the current inside the fluid, which in turn depends on the electric conductivity of the walls. These effects change the pressure drop and heat transfer performance of the system compared with those observed in hydrodynamic conditions.

Despite the existence of certain theoretical and experimental results, presented in the most recent review available in literature by Molokov and Reed (2000) [6], interest in MHD film flow has increased only recently, due to their potential application in LM-PFCs, as the one by Abdou and other researchers at University of California - Los Angeles (UCLA), that designed a flowing liquid metal film concept as inner wall and divertor [7, 8]. The great success of lithium pellet injection experiment in the Tokamak Fusion Test Reactor (TFTR) (1994) has demonstrated the potential of lithium coated limiter and drawn a lot of interest on lithium, since then the research on LM-PFCs has become one of the key topics in fusion [9–11].

Studies performed on the numerical modeling on MHD film flow are much less common than those dealing with a confined flow, where it has been possible to simulate flows with an Hartmann number, a dimensionless number that considers the strength of the magnetic field, equal to 10^4 [12]. To the best of our knowledge, only numerical simulations with significantly lower Hartmann number are present in literature for a MHD free surface flow. Perhaps the first numerical work was carried out by Kudrin (1993) et al. [13], that developed a finite-element solver for fully-developed film flow in a coplanar field. A most recent review was made by Morley (2004) [14] in the context of the APEX project at UCLA, where it was recognized that a numerical tool that can handle complex 3D free surface MHD flows is a necessity to obtain a better understanding of liquid wall flows and would be an extremely valuable aid in the design of LM-PFCs. Initially, efforts were made on developing an MHD module to work with the FLOW3D commercial CFD software package by Huang et al. (2002) [15]. Subsequently, to overcome the limitation of the existing codes, the development of a dedicated code, called HIMAG, was started [16, 17]. Recently, Khodak et al. [18] developed a numerical tool, based on a customized version of ANSYS CFX, capable of simulating flows and heat transfer in an MHD free-surface flow, modelling the gravity-driven flows of LM along the first wall of the proposed Fusion Nuclear Science Facility (FNSF) [19].

A well-known MHD effect is the dampening of velocity oscillations and, more in general, turbulent structures. These can potentially harm the PFC integrity due to heat transfer degradation. To counteract this issue, various surface topologies have been proposed to increase the disturbance in the fluids and enhance convective heat transfer, mostly focused on the wall conductivity dependence of the Lorentz force caused by MHD effects. Huang proposed a hemispherical protrusion wall based on the vortex induction [20] and investigated the heat transfer improvement by applying some electrically conductive ribbons aligned with the main flow direction, called “stripes”, on the insulated back wall of the chute [21]. Recently, Kawamoto studied a structure of partially insulated fins perpendicular to the divertor plate [22]. All of these studies have shown that working on the electrical conductivity of the wall can effectively enhance heat transfer by generating disturbance in the fluid and high-velocity region near the free surface.

This paper investigates a single-phase MHD thin-film flow with the commercial CFD code ANSYS CFX 18.2, validating CFX through a theoretical solution up to $Ha = 1000$ [23] for the case of the insulated wall. The second part of the paper investigates a prototypical case in the framework of LM-PFCs, that is a chute with non-uniform electrical conductivity, for both the back and lateral walls, parallel to the stream direction.

2. Numerical model Figure 1a shows the computational domain: a rectangular and horizontal open channel characterized by a length L in the streamwise direction x, a width W in z direction that is the direction of the applied magnetic field $\boldsymbol{B}$ and a uniform thickness H in the y direction, aligned with the gravity acceleration $-g$. The origin of the coordinate system is placed at the center of the model. The characteristic geometry parameter is the film aspect ratio $\alpha^* = H/W$. The single-phase, isothermal, steady and fully developed flow of liquid lithium ($\rho = 502\ kg/m^3,\ \mu = 5.08 \cdot 10^{-4}\ Pa\,s,\ \sigma = 3.34 \cdot 10^6\ S/m$ [24]) flows through the uniform and perfectly coplanar magnetic field $\boldsymbol{B}$.

2.1 ***Governing equations and dimensionless groups*** The MHD governing equations in ANSYS CFX 18.2 are implemented introducing a body force source term in the momentum equation (Lorentz force) and a formulation based on additional equations for the electric scalar potential φ [25, 26]. Under the assumptions considered in this work, the inductionless approximation is applicable and, therefore, the dimensionless governing equations used by the code are expressed as

$$\frac{1}{N}\left[\frac{\partial \boldsymbol{u}}{\partial t} + (\boldsymbol{u}\cdot\nabla)\boldsymbol{u}\right] = -\nabla p + \frac{1}{Ha^2}\nabla^2\boldsymbol{u} + \boldsymbol{j}\times\boldsymbol{B} + \boldsymbol{S_M} \tag{1}$$

$$\boldsymbol{j} = -\nabla\varphi + \boldsymbol{u}\times\boldsymbol{B} \tag{2}$$

$$\nabla^2\varphi = \nabla\cdot(\boldsymbol{u}\times\boldsymbol{B}) \tag{3}$$

where p is the pressure, $\boldsymbol{u}$ the velocity field, $\boldsymbol{j}$ the current density field, L_c the characteristic length (half-width of the channel $W/2$), and $\boldsymbol{S_M} = \rho\boldsymbol{g}$ is a "general momentum source" that models the gravity effects that would not be simulated otherwise by the CFX buoyancy model because of the absence of density difference and isothermal assumption. The interaction parameter $N = \sigma L_c B_0^2/\rho u_0$ gives the ratio of the electromagnetic forces to the inertia forces, the Hartmann number $Ha = L_c B_0\sqrt{\sigma/\mu}$ represents the ratio of the electromagnetic forces to the viscous forces and characterizes the boundary layer. B_0 and u_0 are respectively the applied magnetic field and the mean velocity. The scaled variables of interest are [25]: the scaled pressure $p_0 = \rho u_0^2$, the scaled electric potential $\phi_0 = L_c u_0 B_0$, the scaled electric current density $j_0 = \sigma u_0 B_0$ and the scaled Lorentz force $F_{L0} = \sigma u_0 B_0^2$. In all the following simulation u_0 is equal to 0.0625 m/s. At the walls perpendicular to $\boldsymbol{B}$ the boundary layers (Hartmann layer) width is $\delta_H = L_c/Ha$, at the walls parallel to $\boldsymbol{B}$ the boundary layer (side layer) width is $\delta_S = L_c/\sqrt{Ha}$ (Figure 1b).

2.2 ***Numerical strategy*** The simulations were performed with the "high-resolution" advection scheme, using a single fluid domain. Since $N >> 1$, all the simulations were carried as a laminar flow. All the simulations have been initialized with the respective hydrodynamic solutions to facilitate the convergence. Figure 1a shows the boundary conditions (BCs). No-slip boundary condition ($\boldsymbol{u} = \boldsymbol{0}$) was used for all the walls except for the top wall, where the free-slip BC is imposed to model the free surface (shear stress $\tau = 0$). To get a fully-developed flow, translation periodicity BCs with the control of the mass flow rate ($\Gamma_i = \Gamma_o$, $u_{average} = u_0$) was established between the inlet and outlet surfaces. Zero electric flux BC (i.e. $\partial\phi/\partial n = 0$) is employed to model a perfectly insulated wall (or wall section), whereas the ground BC ($\phi = 0$) is used for a perfectly conductive wall (or section). A non-uniform,

structured, hexahedral mesh is used, refining the resolution to resolve the Hartmann and side boundary layer (see Figure 1b).

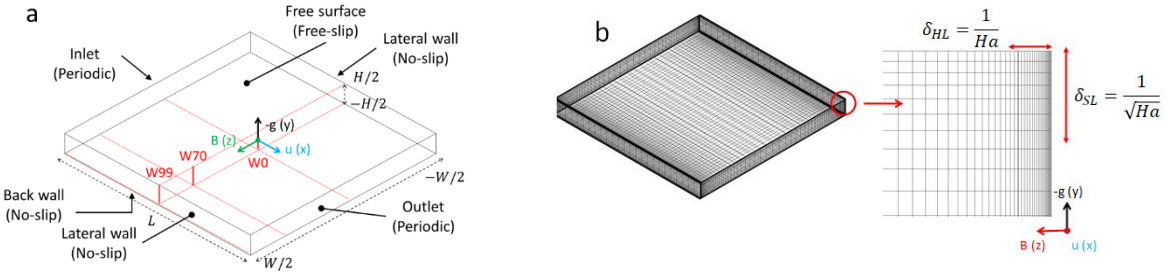

Figure 1: a) Computational domain, BCs and sampling data locations (W0, W70, W99); b) Global mesh and detail of the lateral wall.

3. Model validation The model validation for the insulated case was performed using the theoretical solution provided by Shishko et al. [27] which provides the scaled velocity distribution along the film thickness (y-axis), considering the origin of the coordinate system at the center of the model, therefore $-\frac{H}{2} \leq y \leq \frac{H}{2}$. Shishko employed the approximate variation Galerkin-Kantorovich method as done by Sidorenkov for a rectangular bounded channel [28] that allows to come up with a relatively simple theoretical solution using two basic functions in the z-direction, the parabola and the Hartmann profile. As stated by Molokov [6], this method is not especially accurate, because of a low number of the trial functions, but perhaps is the most significant theoretical results for liquid metal film flows.

The quality of the numerical results was evaluated by comparing the integral of the velocity distribution through the thickness of the film at three different channel positions along $x = 0$: center (W0), 70% (W70) and 99% (W99) of the half-width, as shown in Figure 1a.

3.1 ***Mesh sensitivity study*** A mesh sensitivity study for $Ha = 500$ with $a^* = 0.03$ (W=100 mm, A) and $a^* = 0.044$ (W=90 mm, B) was carried out to analyze the effect of the mesh resolution in the MHD layers. Table 1 shows the results overview. Between 15 and 20 elements in the Hartmann layer (N_H) are required to have a good agreement with the reference solution. A finer resolution (A3) does not bring any significant improvement and, surprisingly, could lead to increased error in some cases (B3). It should be noted that CFX usually requires about 8 elements in the Hartmann layer for the treatment of insulated bounded flows, as it was demonstrated, for instance, in Refs. [29, 30]. Motivating this difference in behavior of the numerical model is not simple, but it could be related to the use of a free-slip BCs. Regarding the side layer resolution (N_S), between 20 and 30 elements are required with, again, a possible degradation of the results observed for higher resolution [23]. The same resolution is usually required by CFX for the simulation of bounded flows [30].

3.2 ***Parametric study*** Since the velocity profiles are sensitive to both the variation of the geometry (α^*) and to imposed magnetic field (Ha), a parametric study was carried out in the range $0.044 \leq a^* \leq 0.2$ and $500 \leq Ha \leq 2000$ (Table 2). A mesh with 20 elements both in the Hartmann and side layer thickness is employed. The errors obtained are quite limited up to $Ha = 1000$, whereas it was impossible to obtain a convergent solution for $Ha = 2000$.

Figure 2 shows the scaled velocity distributions u/u_0 along the y-axis, as a function of y/L_c for all the cases reported in Table 2 along with the sampling positions reported in Figure 1a. The thin line represents the reference solution provided by Shishko [27] while the thick one represents the solution provided by CFX. An increase in Ha correspond with the progressive definition of a core region at the film center, where a quasi-slug flow with a flow rate almost

equal to the mean flow rate is observed, and with the appearance of the well-known Hartmann layers on the lateral walls, with a thickness $\delta_H = L_c/Ha$, and of the side layer on the back wall, with a thickness $\delta_S = L_c/\sqrt{Ha}$ (Figure 2D). Similarly, an increase of α^* with a fixed Ha, corresponds to an increase of the MHD effects through the flow. This behavior can be explained due to the increase in the "active length" of the currents path, with respect to the "passive length", with the film aspect ratio α^* (Figure 2 A, B, C).

As shown in Figure 2, the numerical solution agrees well with the reference one, except near the free surface. This discrepancy is observed on all the three sample lines and it could be attributed to two distinct causes. As mentioned above, the reference solution is derived from an approximate numerical method and, therefore, it is not completely accurate, at least not as much as analytical solutions obtained with less demanding assumptions like, for instance, the Shercliff one [6, 31]. Furthermore, the Shishko theoretical relation is developed under the condition $Ha \gg 1$. Even if large $Ha = 500 \div 1000$ may not fully satisfy this assumption and, therefore, it is conceivable that the discrepancy we observe may be caused by this deviation from the ideal condition of $Ha \to \infty$. Indeed, it can be seen how the deviation between the numerical result and the reference solution is reduced passing from $Ha = 500$ to $Ha = 1000$. Nevertheless, it can be said with confidence that the code is able to recreate all of the fundamental features of the MHD flow and, therefore, it is suitable to perform numerical analyses to support the design of LM-PFCs up to $Ha = 1000$.

Table 1: Mesh information and results for the mesh sensitivity

	N_S	N_H	N. of elements	W0 Error (%)	W70 Error (%)	W99 Error (%)
A1	30	17	96 000	6.7	8.1	11.0
A2	37	17	118 400	8.7	9.8	8.5
A3	30	35	120 000	6.8	8.2	11.0
B1	20	15	110 880	6.2	3.8	8.4
B2	30	20	181 440	6.0	3.9	8.4
B3	60	58	725 760	15.3	15.5	33.0

Table 2: Results of the parametric study

	Ha	α^*	$W(mm)$	W0 Error (%)	W70 Error (%)	W99 Error (%)
A	500	0.044	90	6.0	3.9	8.4
B	500	0.2	50	3.9	2.4	2.4
C	500	0.1	50	7.2	4.7	4.3
D	1000	0.1	50	1.8	4.1	4.1
E	2000	0.1	50	Did not converge		

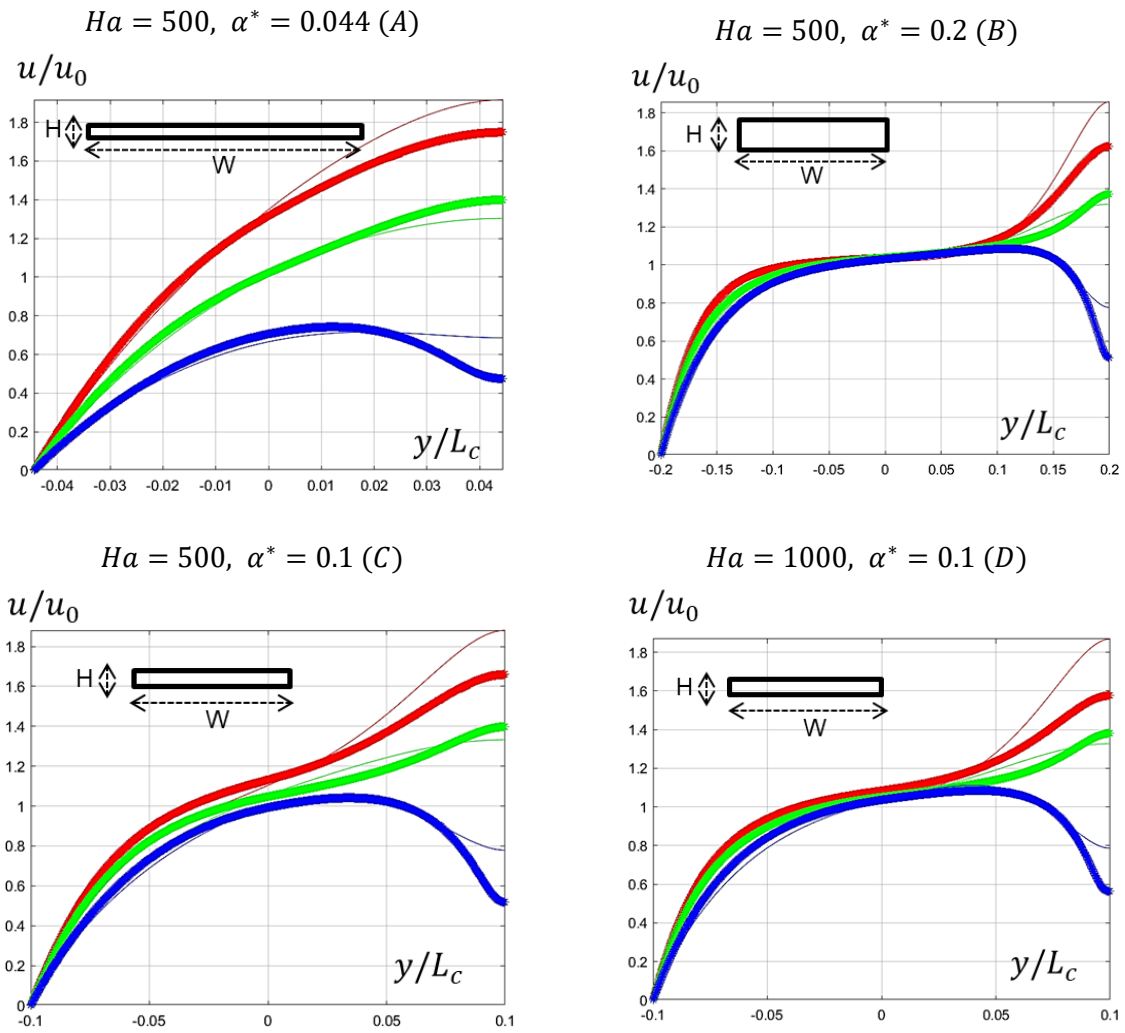

Figure 2: Scaled velocity distribution for cases A, B, C and D. The red line corresponds to the W0 position, the green one with the W70 position and the blue one with the W99 position (Fig. 1a). The thin line is the reference solution, the thick one the CFX solution.

4. Non-uniform wall electrical conductivity study A chute with $\alpha^* = 0.1$ ($W = 50\ mm, H = 5\ mm, L = 50\ mm$) and for $Ha = 300$ is investigated to describe the flow for the case of uniform and non-uniform wall electrical conductivity. Non-uniformity is obtained by placing perfectly conductive strips on the perfectly insulated wall, as shown on Figure 3 where the red color indicates the insulated portion of the wall while the blue color the conductive portion. For the uniform case, perfectly insulating (#1) and conductive walls (#2) are considered and used as a reference for the analysis performed on the non-uniform configurations. Regarding the non-uniform study, several configurations have been considered, which are presented in Figure 3. Test cases #3 and #4 feature insulated lateral walls, and one and three conductive strips on the back wall, respectively. Test cases from #5 to #9 feature an insulated back wall and different strips position on the lateral wall: on the center with two different size (#5, #6), on the upper corners (#7), on the lower corners (#8) and on all the corners (#9). Finally, it has been considered the case with perfectly conductive lateral walls and an insulated back wall (#10). Table 3 shows the results of this study, which are compared with those for hydrodynamic conditions (#0), where $u_{FS}^* = u_{FS}/u_0$ is the dimensionless velocity peak of the free surface and $\Delta p^* = \Delta p/p_0$ is the dimensionless pressure drop. It's useful to introduce the

ratio of the conductive area to the total area for the lateral wall $\xi_{LW} = A_{LC}/A_L$, for the back wall $\xi_{BW} = A_{BC}/A_B$ and for the total surface $\xi_{TOT} = A_L + A_B$, where A_L and A_B are the surface of respectively the lateral and back wall and the subscript "C" denotes the conductive section in the respective surfaces. It was used a mesh with the same layout described in Section 2.2 with, in addition, 20 elements in the proximity of the electrical discontinuity.

In general, and as pointed out by Shishko in [27], it has been observed that when the lateral wall is insulated, the electrical conductivity of the back wall has negligible effects on the flow characteristics. On the other hand, a conductive lateral wall greatly influences the flow structure and, in this case, the conductivity of the back wall has a much more relevant effect on the flow. When the lateral walls are conductive may exist two different flow regimes dependent on the values of the thickness of the film, flow rate, Hartmann number and the thickness and electrical conductivity of the walls. For large Hartmann number, beyond a critical value, the "slow regime" occurs, characterized by strong non-uniformity velocity distribution where there is virtually no movement of the liquid metal in the core and the entire flow is carried by two jets formed near the back wall and the free surface. For small Ha, the regime becomes "fast" and its characterized by a monotonic velocity profiles through the thickness of the film [27]. Due to the values of the parameters in this study, only the fast regime occurs.

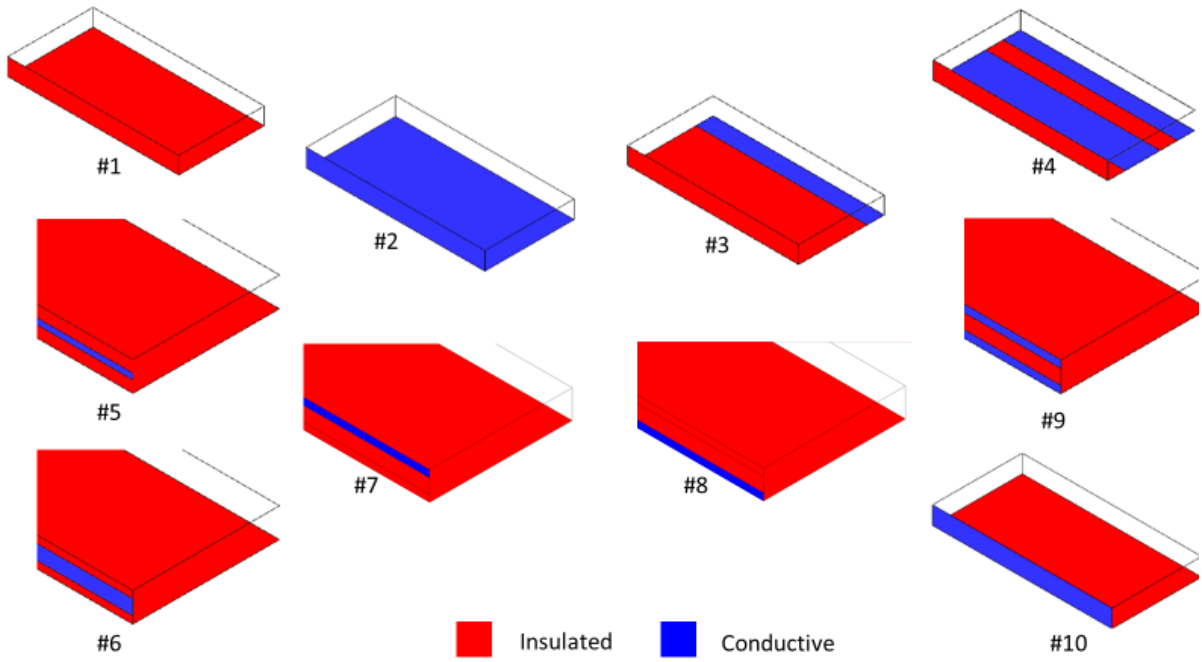

Figure 3: Cases of the electrical non-uniformity conductivity study. Due to symmetry, only half of the channels is represented.

Table 3: Results of wall electrical conductivity study

	#0	**#1**	**#2**	**#3**	**#4**	**#5**	**#6**	**#7**	**#8**	**#9**	**#10**
ξ_{LW}	0	0	1	0	0	0.2	0.5	0.250	0.250	0.5	1
ξ_{BW}	0	0	1	0.20	0.60	0	0	0	0	0	0
ξ_{TOT}	0	0	1	0.182	0.545	0.018	0.045	0.023	0.023	0.045	0.091
Δp^*	0.014	0.304	2.328	0.304	0.311	0.433	0.777	0.389	0.322	1.221	1.257
u^*_{FS}	1.72	1.74	3.99	1.74	1.76	1.95	2.30	1.84	1.84	2.77	2.66

4.1 ***Uniform wall electrical conductivity*** Figure 4 and Figure 5 show the scaled velocity distribution u/u_0 and the scaled current density streamlines and electric potential distribution on the half cross-section respectively for the insulated case (#1) and the conductive case (#2). In the case of the insulated chute (Figure 4), the currents close in the thin Hartmann boundary layer and u_{FS}^* is found to be close to its hydrodynamic value (#0), whereas the pressure drop is about 20 times more (see Table 3), since at the hydrodynamic pressure loss is added the MHD pressure loss. The absence of the no-slip condition on the free surface, that can be considered a side wall for the MHD phenomenon, results in a non-uniform distribution of the electric potential in the magnetic field direction (Figure 4). This behavior, which does not occur for the analogous insulated bounded flow, results in a non-specular distribution of the electric currents with respect to the average plane between the back wall and the free surface (dashed line in Figure 4 down). This causes the current loops to be shifted toward the free surface close to the Hartmann wall. This causes a Lorentz force that, as in the analogous bounded flow, is opposite to the pressure gradient in almost all the cross-section but, unlike the confined case, is not symmetrical near the side wall with respect to this plane (Figure 6 up detail) and causes the peculiar the velocity distribution close at the corner between the lateral wall and the free surface (Figure 4).

The presence of the conductive walls changes the electric potential distribution and increase the potential difference between the walls, at which $\phi = 0$ due to the perfectly conducting assumption, and the free surface (Figure 5). The electric currents flow through the walls and tend to close preferentially through the back wall. Since the free surface does not allow the currents to cross the boundary, these are aligned with the magnetic field there and close through the boundary layer, where they assume the greatest intensity (Figure 5). This causes a different Lorentz force distribution on the cross-section compared to the insulated case (Figure 6), which opposes the pressure gradient almost everywhere but assume an increasingly smaller value as it approaches the free surface, where it becomes positive and an intense jet is formed (Figure 5). It is important to note that the Lorentz force opposes the pressure gradient also near the lateral wall, because the current there is almost aligned with the magnetic field, and this cause a change in the Hartmann layer structure (Figure 5), which appears to be no longer characterized by $\delta_H = L_c/Ha$, like it is instead the case for #1 and its analogous bounded case, the Shercliff flow. This behavior has been described already by Shishko [27], who considered this case theoretically, but it appears to have no parallel with the analogous bounded flow, the Uflyand flow, in which all the bounding walls are perfectly conductive [32]. It is reasonable to assume that this difference is related to the presence of the free surface, which behaves like a perfectly insulating wall in our case and in the one considered by Shishko, whereas in the Uflyand flow the opposite perfectly conductive wall allows the exchange of currents between the side walls, which prevents the formation of this characteristic boundary layer. Furthermore, for the preservation of the flow rate, the great intensity of the free surface jet causes a counter flow area near the back wall, which is marked in Figure 5 with a red cross. The pressure drop and the peak of the free surface velocity are respectively 170 and 2.3 higher with respect to #0 case (Table 3).

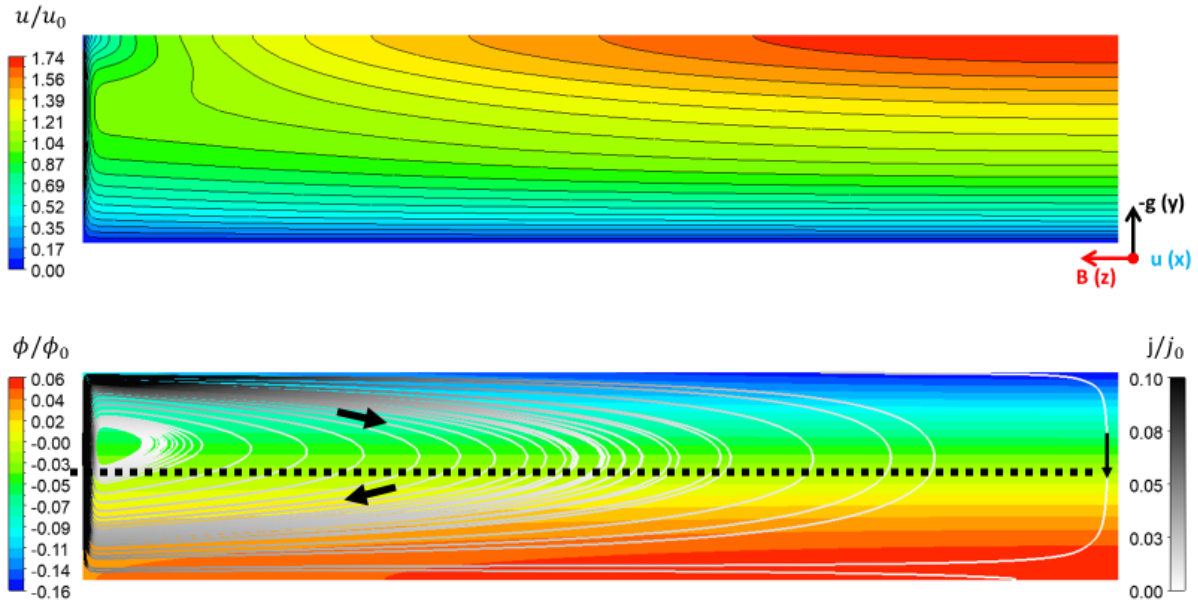

Figure 4: Scaled velocity distribution (up) and scaled current density streamlines and electric potential distribution (down) on the half-cross section for the insulated (#1) case. The dashed represent the average plane between the back wall and the free surface.

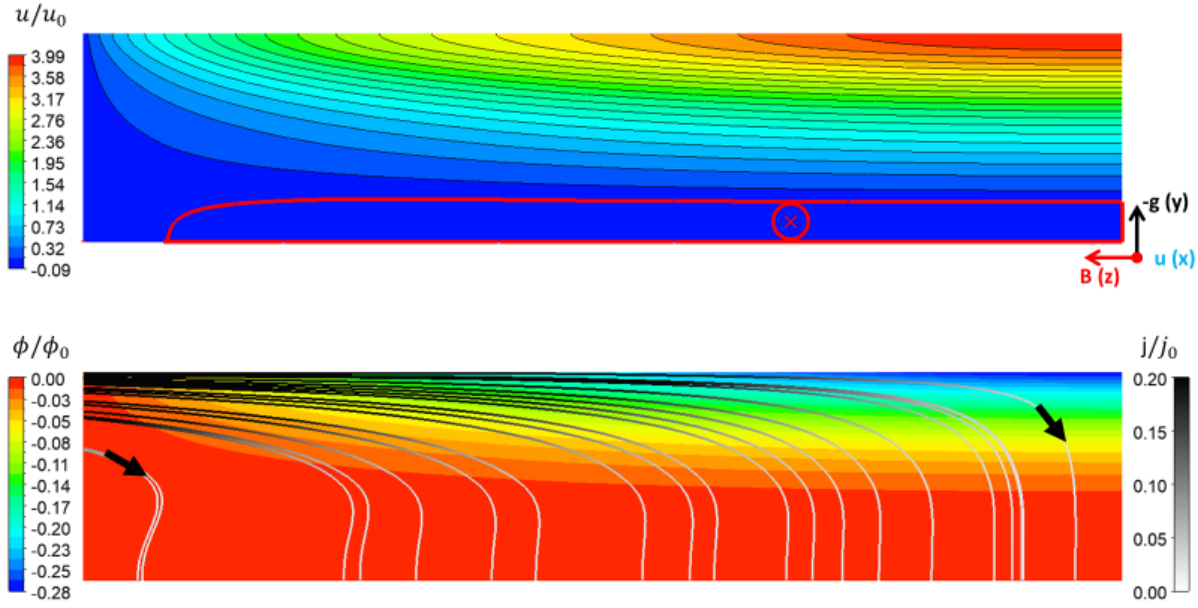

Figure 5: Velocity distribution (up) and current density streamline and electric potential distribution (down) on the half-cross section for the conductive (#2) case. The red cross in the upper figure mark the counter flow zone.

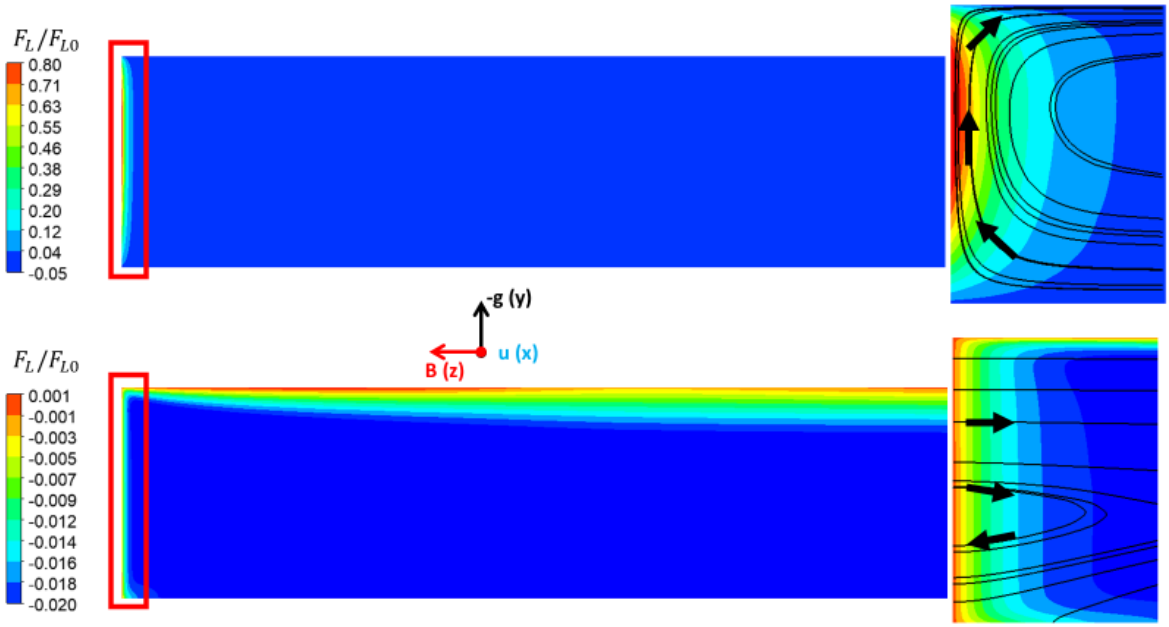

Figure 6: Lorentz force distribution on the half-cross section and detail of current streamlines in the Hartmann layer: perfectly insulated #1 (up) and conductive case #2 (down)

4.2 ***Non-uniform wall electrical conductivity*** In this case, the effect on the flow of partially conductive back and lateral walls is investigated by applying several configurations of perfectly conductive strips (Figure 3), represented with a blue line in Figure 7, Figure 8 , Figure 9 and Figure 10. In these figures, the velocity distribution u/u_0, the current density streamlines and the electric potential distribution on the half cross-section are shown, respectively, for the #4, #6, #9 and #10 cases.

When the lateral wall is insulated, the electrical conductivity of the back wall is found to have a negligible effect on the global flow, as observed by Shishko [27] and similar to what is known for the analogous bounded flow [25]. Indeed, the distribution of the electric potential across the cross-section is quite similar with respect to the insulated case #1 (cfr. Figure 4 and Figure 7), where the maximum value is assumed near the perfectly conductive strips and is therefore equal to 0. The currents flow through the back wall conductive strips (Figure 7) but in the remaining part of the cross-section their distribution is practically equivalent to the insulated case and therefore produces the same distribution of the Lorentz force, justifying the negligible effect of the electrical conductivity of the back wall. The pressure drop and u_{FS}^* are quite similar in the cases #1, #3 and #4, as shown in Table 3, even if the back plate in #4 features 60% of its surface as perfectly conductive.

Contrariwise, when the lateral wall is conductive, more interesting phenomena appear. It is important to note that the percentage of the conductive surface area on the Hartmann (lateral) wall greatly influences the velocity distribution (Figures 8, 9 and 10): both the free surface velocity and pressure drop increase with this parameter. It is interesting to note that not only the percentage of the conductive portion of the lateral wall (ξ_{LW}) is relevant, but also the location of that portion: indeed both the #6 and #9 case have the same lateral plate conductive portion ($\xi_{LW} = 0.5$), but the values of the free surface peak velocity and pressure drop are higher for the latter (Table 3), in which the conductive strips are placed close to the free surface and back wall. This can also be partially observed between case #7 and #8, where the lower percentage of the conductive surface on the lateral wall ($\xi_{LW} = 0.25$), generates an increase in the pressure drop only when the conductive corners are placed close to the free surface. The distribution of the electric potential is quite similar between the #6 and #9 cases, and they both

do not differentiate much from the insulated #1 case, but the currents flow through the conductive strips (Figure 8 and 9 down) that, being placed in a different position, cause the onset of a very different distribution of the Lorentz force in these two cases.

The case #6 Lorentz force distribution is analogous to #1 (cfr. Figure 6 up with Figure 11 up), except for the region close to the conductive section. The Lorentz force is aligned with the pressure gradient in proximity of the insulated portion of the lateral wall, where the currents flow through the Hartmann layer, but is opposing it near the conductive strip. This phenomenon smooths the velocity gradient between the no-slip BC and the core velocity, and changing the Hartmann layer structure, with a similar mechanism to that observed in case #2 (Figure 5). In fact, close to the conductive wall, the flow is almost stagnant, but the classical Hartmann layer is, instead maintained at the wall insulated sections (Figure 8), generating a strong velocity gradient on the y-direction.

Instead, case #9 shows a very different Lorentz force distribution, due to the inversion of the current ($-y$ direction) in the proximity of the lower conductive wall section (Figure 11 down). This causes the velocity distribution shows in Figure 9, where a counter flow zone generated in that region and the Hartmann layer structure reappears only near the insulated portion. The structure of the free surface jet is nearly unchanged compared with #2 thanks to the effect of the upper corner conductive wall section.

The weak influence of the back wall conductivity on the flow features, indeed relevant only when also the lateral wall is conductive, can be seen comparing case #2 and case #10 (cfr. Figure 5 and 10). Indeed, when only the lateral wall is conductive, the electric potential distribution is like the insulated #1 case since the ground BC for the potential on the back wall is removed. This situation causes a similar distribution of the currents in the cross-section (Figure 10 down) with the exception in the proximity of the lateral wall, where in this case the currents flow through the conductive wall rather than in the Hartmann layer. The distribution of the Lorentz force, showed in Figure 12, explain the absence of the counter flow near the back wall for this case, since the Lorentz force in that position does not oppose the pressure gradient and the free surface jet is quite smaller compared with #2.

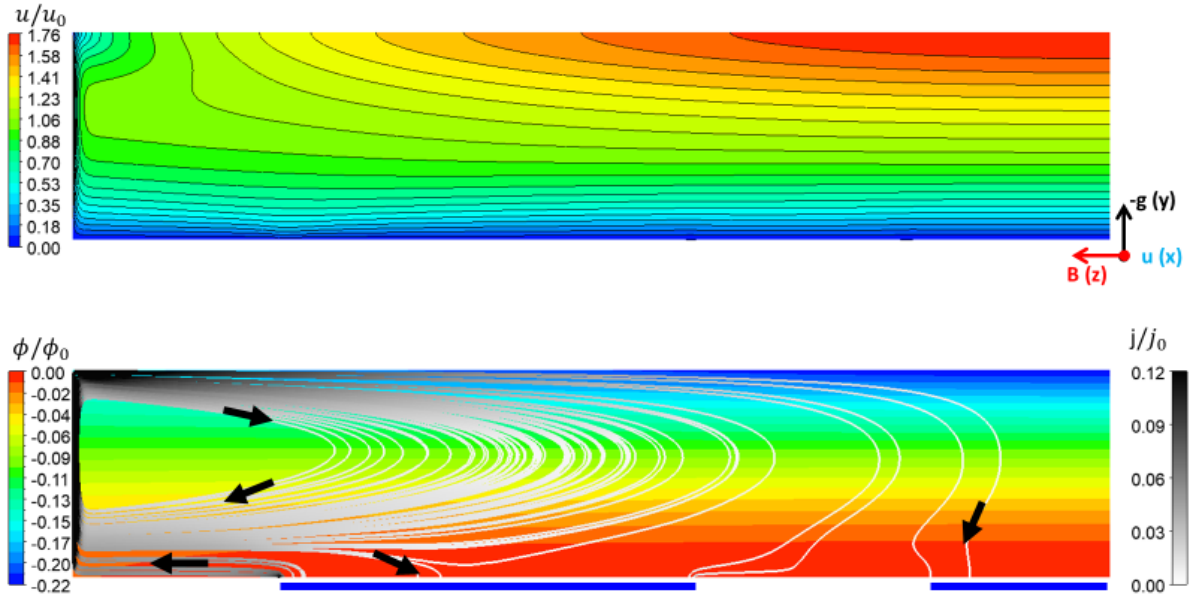

Figure 7: Velocity distribution (up), current density streamlines and electric potential distribution (down) on the half cross-section for the #4 case.

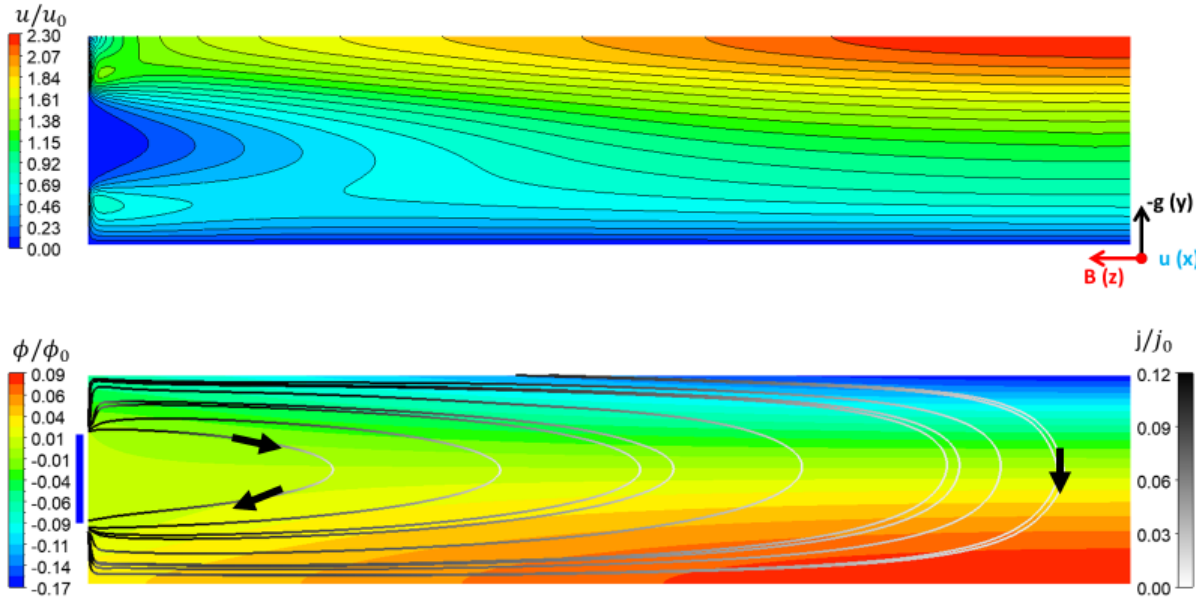

Figure 8: Velocity distribution (up), current density streamlines and electric potential distribution (down) on the half cross-section for the #6 case.

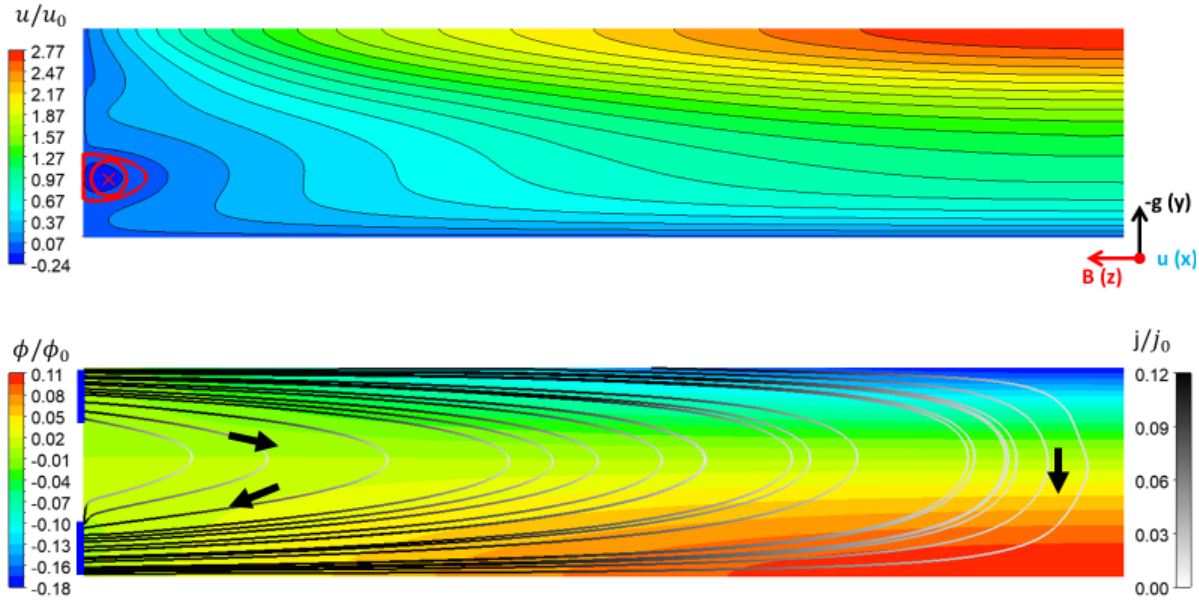

Figure 9: Velocity distribution (up), current density streamlines and electric potential distribution (down) on the half cross-section for the #9 case. The red cross in the upper figure mark the counter flow zone.

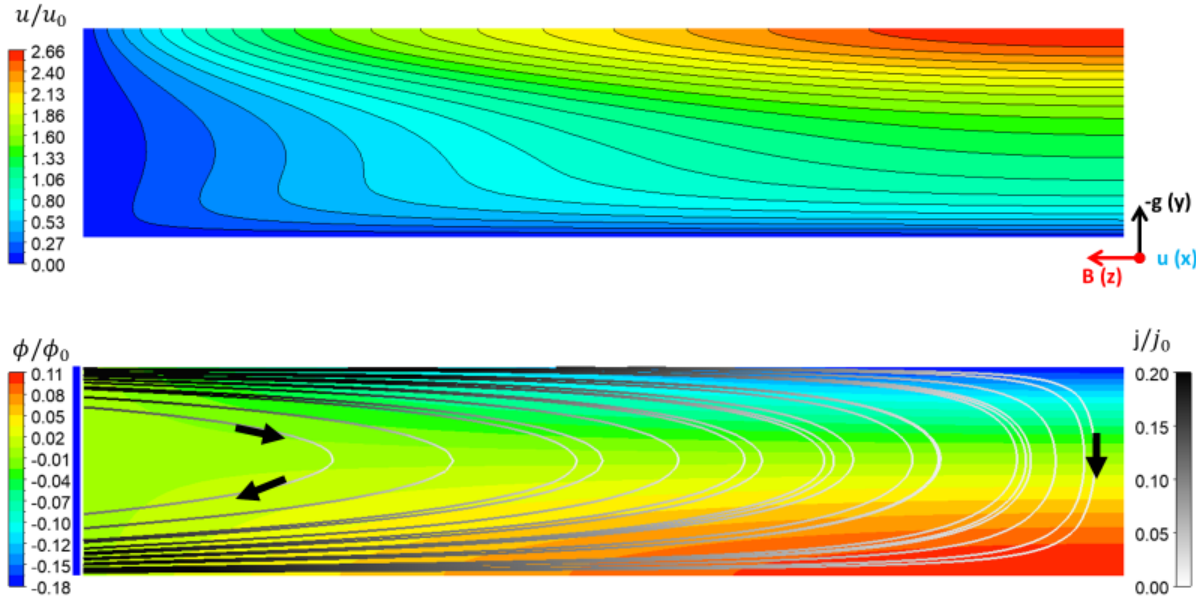

Figure 10: Velocity distribution (up), current density streamlines and electric potential distribution (down) on the half cross-section for the #10 case.

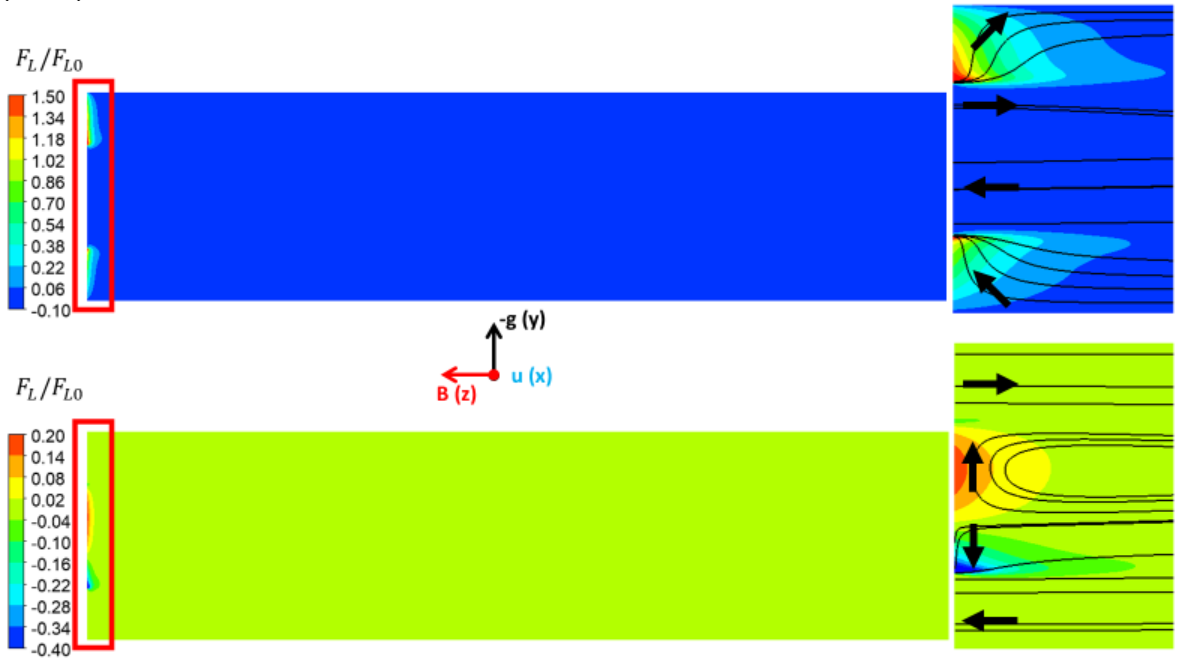

Figure 11: Lorentz force distribution on the half-cross section for the #6 case (up) and #/9 case (down). Detail of the force distribution close to the Hartmann wall and current streamlines.

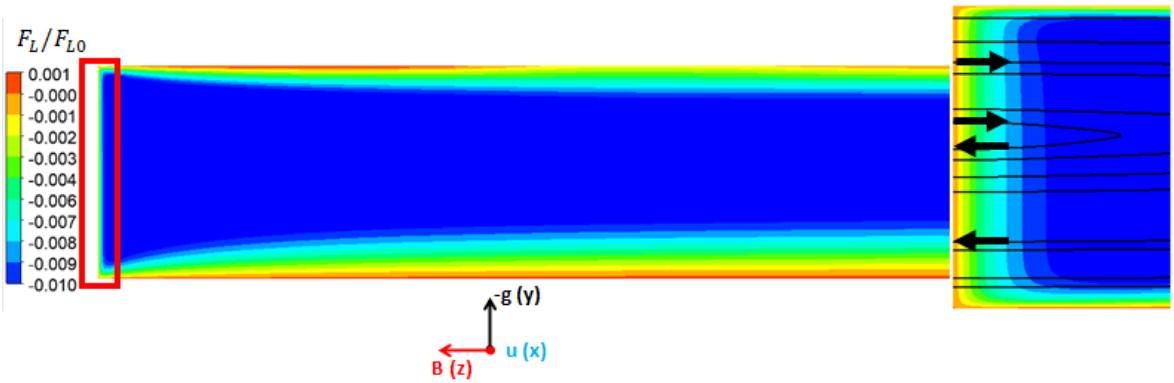

Figure 12: Lorentz force distribution on the half-cross section for the #10 case (up). Detail of the force distribution close to the Hartmann wall and current streamlines.

4.3 ***Effect of wall conductivity on free surface velocity promotion*** As it is shown in Table 3, the peak velocity of the free surface is greatly modified depending on the layout considered for the chute and lateral wall. It could be argued that a high velocity of the film close to the free surface is beneficial for fusion applications, both in divertors and flowing first walls, since it allows for a faster recycling of the liquid armor. Unfortunately, conductive walls and substrate comes with a significant pressure penalty compared with the baseline insulated case. From the point of view of LM-PFC design, the question is what chute layout is the most efficient at maximizing the free surface velocity without introducing too large of a pressure penalty.

The parameter u_{FS}^* is maximized for #2, featuring uniform perfectly conducting walls, where the velocity is more than doubled compared with #1. Unfortunately, this is accomplished with a 666% increase in pressure loss, which is likely not acceptable. Moreover, the large flow reversal close to the back wall is harmful for the potential for tritium accumulation and could cause issues for liquid recycling and heat removal. Looking at Table 3, we find that three other cases have a significant increase of u_{FS}^* ($> 30\%$ compared with #1): #6, #9, and #10. Among these, #10 can be discarded, since it has a slightly higher pressure penalty compared with #9, but lower free surface velocity. Both cases #6 and #9 feature half of the Hartmann wall surface as conductive, with the latter performing better in free surface promotion ($+32\%$ versus $+59\%$), and are characterized by a quite large pressure penalty ($+155\%$ against $+300\%$). The flow reversal observed in #9 is not a desired feature, for the same reasons of #2, and, therefore, it is possible to conclude that #6 is the best configuration to maximize u_{FS}^*, if relatively large pressure penalty is deemed acceptable.

Even if case #6 is the one where u_{FS}^* features its largest value, it is hardly the most "efficient" in terms of increase of flow promotion per additional pressure loss compared with the perfectly insulated chute. We can define the free surface promotion efficiency as the figure of merit

$$\eta = \frac{\dfrac{[u_{FS}^* - u_{FS}^*(\#1)]}{u_{FS}^*(\#1)}}{\dfrac{[\Delta p^* - \Delta p^*(\#1)]}{\Delta p^*(\#1)}}$$

Where $u_{FS}^*(\#1)$ and $\Delta p^*(\#1)$ are the free surface velocity and pressure loss of the perfectly insulated chute. Larger η corresponds to a higher percentage increase in free surface velocity compared with the corresponding increase in pressure penalty associated to the presence of a conductive surface. In Figure 13**,** it is possible to observe how most cases have $\eta \approx 0.2$, which means that for a 100% increase in pressure loss, a 20% flow promotion is obtained.

The case #8, lower corner conductive, is the most efficient, whereas case #4 and case #5 are other interesting outliers, even if it should be noted that for the former the flow promotion is insignificant ($\approx 1\%$). Therefore, it can be concluded that the chute with a conductive section ($\xi_{LW} = 0.2 - 0.5$) placed in the middle of the Hartmann wall is the most promising configuration in promoting the flow surface velocity, when accounting for both absolute and relative increase weighted against the pressure loss penalty.

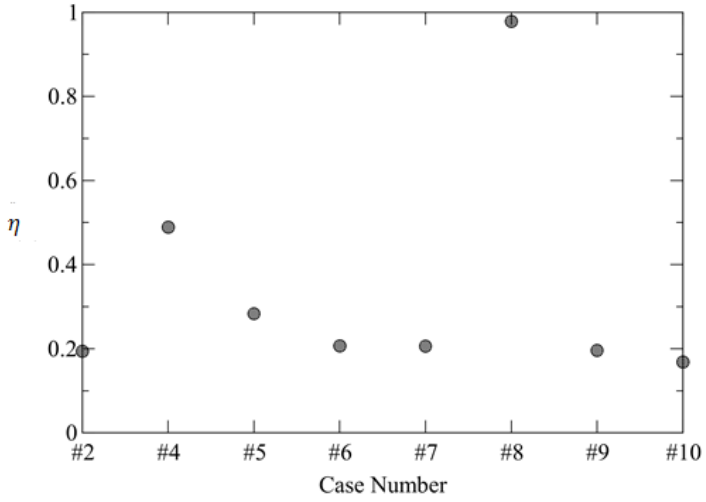

Figure 13: Free surface promotion efficiency (η) for the chutes with $u^*_{FS} - u^*_{FS}(\#1) > 0$.

5. Conclusions The free-slip single-phase thin film MHD flow has been investigated with the Ansys CFX 18.2 code. The numerical model is validated up to $Ha = 1000$ for the case of insulated walls and $0.044 \leq a^* \leq 0.2$. A good agreement is found with the theoretical solution presented by Shishko [27].

Consequently, the flow in a chute with insulating, conductive, and partially conductive walls has been investigated to highlight the effect of discontinuous wall conductivity on the back wall and Hartmann walls. A partially conductive back wall has a negligible effect on the flow where also the lateral wall is insulated, consistently to the analogous bounded case [25], whereas the transition from insulating to conductive Hartmann (lateral) wall causes larger pressure losses, higher free surface velocity, structural change in the Hartmann boundary layer, where $\delta_H \neq O(Ha^{-1})$, and eventually, counterflow. The location of the conductive sections on the Hartmann wall influences the flow features, resulting in higher free surface velocity and pressure drop when these are close to the back wall and free surface. The presence of a conductive back wall, with a conductive lateral wall, have a great influence on the flow characteristics, greatly enhancing the free surface velocity and pressure drop. These phenomena could be interesting for the PFC applications, where increasing the free surface velocity with a contained pressure drop could be an attractive solution. In this case, the best compromise is to have a partially conductive lateral wall with the conductive portion at the center of the wall (case #6), instead of a totally conductive wall (Table 3).

The partially conductive lateral wall configuration (case #5 and #6) should be investigated in a next work considering conductive sections with finite wall conductivity and thickness, in order to approach more realistic conditions that are encountered in the design of LM-PFC. In particular, it would be interesting to confirm if flow promotion performances could be higher for a more realistic case, since it is well known that jet peak velocity in a MHD bounded flow are generally higher for a finite conductivity wall than for a perfectly conducting one [25]. Case #8, conductive lower corner, can also be considered as a candidate for further study due to its high flow promotion efficiency.

From a theoretical point of view, a more in-depth study appears to be warranted to completely characterize the anomalous Hartmann layer structure observed for a conductive Hartmann wall. In particular, case #2 and #9 could benefit by a more thorough investigation to assess the effect of Ha and finite wall conductivity. Onset and extension of flow reversal regions are also a topic of interest and should be characterized in detail.

Acknowledgements This work has been carried out within the framework of the EUROfusion Consortium and has received funding from the Euratom research and training programme 2014-2018 and 2019-2020 under grant agreement No 633053. The views and opinions expressed herein do not necessarily reflect those of the European Commission.

[1] T. Donné, W. Morris, European Research Roadmap to the Realisation of Fusion Energy - Long Version, 2018. https://www.euro-fusion.org/eurofusion/roadmap/.
[2] F.L. Tabarés, Present status of liquid metal research for a fusion reactor, Plasma Phys. Control. Fusion. (2015). https://doi.org/10.1088/0741-3335/58/1/014014.
[3] R.E. Nygren, F.L. Tabarés, Liquid surfaces for fusion plasma facing components - A critical review. Part I: Physics and PSI, Nucl. Mater. Energy. 9 (2016) 6–21.
[4] M.G. Hvasta, E. Kolemen, A.E. Fisher, H. Ji, Demonstrating electromagnetic control of free-surface, liquid-metal flows relevant to fusion reactors, Nucl. Fusion. (2018). https://doi.org/10.1088/1741-4326/aa9344.
[5] J.-C. Yang, T.-Y. Qi, D.-W. Ren, B.-Q. Liu, M.-J. Ni, Surface waves of liquid metal film flow under the influence of spanwise magnetic field, Fusion Eng. Des. 130 (2018) 42–47. https://doi.org/10.1016/j.fusengdes.2018.03.021.
[6] S. Molokov, C.B. Reed, Review of free-surface MHD experiments and modeling., Argonne, IL, 2000. https://doi.org/10.2172/757509.
[7] N.B. Morley, Analysis of thin film liquid metal protection of fusion reactor plasma contact surfaces, UCLA-FNT-40. United States, 1990. https://inis.iaea.org/search/search.aspx?orig_q=RN:23038165.
[8] M.A. Abdou, On the exploration of innovative concepts for fusion chamber technology: APEX interim report. UCLA-ENG-99-206, 1999.
[9] W. Xu, Experimental and numerical analysis of thermoelectric magnetohydrodynamic driven liquid lithium flow in open channels for fusion applications, University of Illinois at Urbana-Champaign, 2015. http://hdl.handle.net/2142/78620.
[10] J.D. Strachan, D.K. Mansfield, M.G. Bell, J. Collins, D. Ernst, K. Hill, J. Hosea, J. Timberlake, M. Ulrickson, J. Terry, E. Marmar, J. Snipes, Wall conditioning experiments on TFTR using impurity pellet injection, J. Nucl. Mater. (1994). https://doi.org/10.1016/0022-3115(94)90314-X.
[11] G.F. Nallo, S. Carli, G. Caruso, F. Crisanti, G. Mazzitelli, L. Savoldi, F. Subba, R. Zanino, Modeling the lithium loop in a liquid metal pool-type divertor, Fusion Eng. Des. 125 (2017) 206–215. https://doi.org/10.1016/j.fusengdes.2017.07.004.
[12] M.J. Ni, R. Munipalli, N.B. Morley, P. Huang, M.A. Abdou, A current density conservative scheme for incompressible MHD flows at a low magnetic Reynolds number. Part I: On a rectangular collocated grid system, J. Comput. Phys. (2007). https://doi.org/10.1016/j.jcp.2007.07.025.
[13] V.M. Kudrin, S.Y. Smolentsev, A. V. Tananaev, Developed flow of a thin liquid metal layer in an inclined magnetic field, Magnetohydrodynamics. 29, No. 1 (1993) 66–70. http://mhd.sal.lv/contents/1993/1/MG.29.1.11.R.html.
[14] N.B. Morley, S. Smolentsev, R. Munipalli, M.-J. Ni, D. Gao, M. Abdou, Progress on the modeling of liquid metal, free surface, MHD flows for fusion liquid walls, Fusion Eng. Des. 72 (2004) 3–34. https://doi.org/10.1016/j.fusengdes.2004.07.013.

[15] H.. Huang, A. Ying, M.. Abdou, 3D MHD free surface fluid flow simulation based on magnetic-field induction equations, Fusion Eng. Des. 63–64 (2002) 361–368. https://doi.org/10.1016/S0920-3796(02)00261-2.
[16] R. Munipalli, V. Shankar, C. Chandler, C. Rowell, M.J. Ni, S. Smolentsev, N. Morley, M.A. Abdou, A. Hadid, Development of a 3-D Incompressible Free Surface MHD Computational Environment for Arbitrary Geometries: HIMAG, 2003.
[17] Ramakanth Munipalli, P.-Y.Huang, C.Chandler, C.Rowell, M.-J.Ni, N.Morley, S.Smolentsev, M.Abdou, Physical Model Development and Benchmarking for MHD Flows in Blanket Design, Argonne, IL (United States), 2008. https://doi.org/10.2172/929194.
[18] A. Khodak, C. Kessel, M. Tillack, Design and Analysis of the Liquid Metal Free-Surface Divertor Cooling System, Fusion Sci. Technol. 75 (2019) 930–938. https://doi.org/10.1080/15361055.2019.1643689.
[19] C.E. Kessel, J.P. Blanchard, A. Davis, L. El-Guebaly, L.M. Garrison, N.M. Ghoniem, P.W. Humrickhouse, Y. Huang, Y. Katoh, A. Khodak, E.P. Marriott, S. Malang, N.B. Morley, G.H. Neilson, J. Rapp, M.E. Rensink, T.D. Rognlien, A.F. Rowcliffe, S. Smolentsev, L.L. Snead, M.S. Tillack, P. Titus, L.M. Waganer, G.M. Wallace, S.J. Wukitch, A. Ying, K. Young, Y. Zhai, Overview of the fusion nuclear science facility, a credible break-in step on the path to fusion energy, Fusion Eng. Des. 135 (2018) 236–270. https://doi.org/10.1016/j.fusengdes.2017.05.081.
[20] H. Huang, B. Li, Heat transfer enhancement of free surface MHD-flow by a protrusion wall, in: Fusion Eng. Des., 2010. https://doi.org/10.1016/j.fusengdes.2010.04.013.
[21] H. Huang, B. Li, Heat Transfer Enhancement of MHD Flow by Conducting Strips on the Insulating Wall, J. Heat Transfer. 133 (2011). https://doi.org/10.1115/1.4002436.
[22] M. Kawamoto, K. Muraoka, S. Ito, H. Hashizume, Heat transfer enhancement in MHD free surface flow by controlling the electromagnetic force with fin structure, Fusion Eng. Des. (2019). https://doi.org/10.1016/j.fusengdes.2019.04.079.
[23] S. Siriano, Numerical study of MHD thin-film flows for Plasma Facing Components: fundamental phenomena and code validation, Sapienza University of Rome, 2018.
[24] H.W. Davison, Compilation of thermophysical properties of liquid lithium, Natl. Aeronaut. Sp. Adm. (1968).
[25] U. Müller, L. Bühler, Magnetofluiddynamics in Channels and Containers, 2001. https://doi.org/10.1007/978-3-662-04405-6.
[26] ANSYS© CFX 18.2, ANSYS CFX-Solver Theory Guide, (2017).
[27] A.Y. Shishko, A theoretical study of steady film flows in a coplanar magnetic field, Magnetohydrodynamics. 28, No. 2 (1992). http://mhd.sal.lv/contents/1992/2/MG.28.2.11.R.html.
[28] S.I. Sidorenkov, A.Y. Shishko, Variational method of calculation of MHD flows in channels with large aspect ratios and conducting walls, Magn. Gidrodin. (1991). http://mhd.sal.lv/contents/1991/4/MG.27.4.14.R.html.
[29] S. Siriano, A. Tassone, G. Caruso, A. Del Nevo, MHD forced convection flow in dielectric and electro-conductive rectangular annuli, Fusion Eng. Des. 159 (2020) 111773. https://doi.org/10.1016/j.fusengdes.2020.111773.
[30] A. Tassone, Study on liquid metal magnetohydrodynamic flows and numerical application to a water-cooled blanket for fusion reactors, Sapienza University of Rome, 2019.
[31] J.A. Shercliff, Steady motion of conducting fluids in pipes under transverse magnetic fields, Math. Proc. Cambridge Philos. Soc. 49 (1953) 136. https://doi.org/10.1017/S0305004100028139.
[32] Y.S. Uflyand, Flow of Conducting Fluid in a Rectangular Channel in a Transverse

Magnetic Field, Sov. Phys. Tech. Phys. 5 (1961) 1194.